Interplay of order and disorder in the optical properties of opal photonic crystals

V. N. Astratov*

*Department of Physics and Optical Science, University of North Carolina at Charlotte, Charlotte, North Carolina 28223
and Department of Physics and Astronomy, University of Sheffield, Sheffield S3 7 RH, United Kingdom*

A. M. Adawi, S. Fricker, M. S. Skolnick, and D. M. Whittaker
Department of Physics and Astronomy, University of Sheffield, Sheffield S3 7RH, United Kingdom

P. N. Pusey

Department of Physics and Astronomy, University of Edinburgh, Edinburgh EH9 3JZ, Scotland

It is shown that the polycrystalline structure of self-assembled synthetic opals leads to an interplay of properties determined by order and disorder in the vicinity of the optical stop band. We analyze the balance of photon fluxes by studying angle-resolved spectra of diffracted and scattered light for all directions in space. It is shown that the shape of the stop band features in different types of optical spectra (diffraction, transmission, and scattering) is interlinked and must be studied jointly to understand optical phenomena in these materials. The principal effects are (i) angular dispersion of the photonic stop bands in diffraction spectra, (ii) inhomogeneous broadening of the stop band in zero-order transmission, and (iii) appearance of very strong peaks in the spectra of scattered light, with resonant enhancements observed with intensity up to ~10 times greater than background scattering levels. It is shown that the resonant enhancements arise from multiple incoherent backward/forward reflections between the microcrystallites. It is shown that the spatial pattern and spectral form of the scattering spectra can be deduced from the analysis of angle-resolved zero-order transmission spectra under conditions where the attenuation length of light within the stop band is comparable to the thickness of the sample. The methodology of the studies developed in this paper is applicable to a wide class of disordered photonic crystal structures.

I. INTRODUCTION

Synthetic opals are self-assembled three-dimensional (3D) photonic crystal structures with photonic band gaps in the visible wavelength range.[1–6] In the same way as natural opals are formed, with their well-known play of colors,[7] synthetic opals are formed by submicron silica spheres packed into a relatively regular fcc lattice.[8] An attractive feature of synthetic opals, in comparison with their natural counterparts, arises from the possibility to use the lattice of spheres as a template that can be infiltrated with a variety of ferroelectric, nonlinear, and photorefractive materials, thus permitting the creation of *composites* for optoelectronic applications. Recently opals were infiltrated with semiconductors,[1,2,9–13] titanium dioxide,[14–16] graphite,[17] liquid crystals,[18,19] conjugated polymers,[20,21] organic-inorganic layered perovskites,[22] $BaTiO_3$,[23] chalcogenide glasses,[24] SnS_2,[25] and VO_2.[26]

In much of this work it was realized that the photonic crystal properties of the composite materials are strongly dependent on the quality of ordering of the initial opal template. Best ordering can be achieved in materials that are only a few monolayers thick where the self-assembly of spheres can be controlled by the use of patterned[27–29] substrates or by vertical deposition techniques.[30–35] Obtaining thicker materials (>10 μm) typically relies on the standard method[1–6] of sedimentation of spheres from suspension. This method, however, generates *disorder* in a variety of forms. In general the types of disorder in sedimented opals are similar

to the textbook examples of disorder in crystalline lattices of solid-state systems, with a scaling factor for silica spheres that is ~10^3 times larger than the size of typical atoms. These include stacking faults,[36] dislocations, and point defects,[37] as well as domains[36,38,39] of various orientations and sizes. Stacking faults or random arrows in the sequence of layers along the direction of sedimentation such as $ABCABABC\ldots$ (the fcc lattice is characterized by the $ABCABC\ldots$ sequence) are one of the most common types of defect, with densities reaching ~10% in sedimented bulk opals[36] and ~1% in films a few monolayers thick.[35] The concentration of point defects typically varies from ~10^{-2} defect per unit cell in sedimented opals[36] to ~10^{-3} in the thin films.[35]

The formation of domains of unknown size and orientation[36,38,39] constitutes a type of disorder intrinsically inherent to self-assembly. The mechanism of formation of domains as well as of various defects in sedimented opals is not very well understood up to the present time. However, it is likely that the top interface of the sediment grows by aggregation of silica spheres, which after reaching the growing surface by gravity, relax to minimum potential-energy sites within a hard-sphere interaction potential.[38] (This technique of colloidal epitaxy differs from crystallization in thermodynamical equilibrium, which occurs in the volume of the concentrated colloidal dispersions in normal gravity[40–42] or in microgravity[43,44] conditions). On an empirical level the ordering of the lattice is influenced by many factors including the width of the size distribution of spheres (standard devia-

tion 3%–5%), the concentration of the suspension, flatness of the substrate, the height of the sediment, *et al.* These factors lead to variable parameters of the domain structure in different samples. It is important to stress, however, that the very existence of domains in the sedimented opals with the sizes in the centimeter scale[1–6] is *inevitable* in practice in presently available preparation techniques.

From the theoretical standpoint the optical properties of disordered photonic crystals have attracted considerable interest, particularly with regard to the major goals in the field such as realization of complete photonic band gaps[45] (PBG) and strong localization of light.[46] The disorder leads to the appearance of localized states in the region of the gap and band edges thus closing the complete band gap.[47–50] It has been theoretically shown[49] that in the inverted opal structure the band gap closes for fluctuation of lattice constants as small as 2% due to the extreme sensitivity of high-frequency bands to the presence of disorder. At the same time disorder can help[46] to achieve strong localization of light at the stop band edges. The experimental observation of strong localization phenomena is, however, made extremely difficult because of the effects of residual absorption and the large refractive index contrasts required.

Experimental studies of the effects of disorder on the optical properties of photonic crystals are rather few in number, partly due to difficulties in controlling[51] the type and amount of disorder in self-assembled materials. Most often effects related to disorder are encountered in the course of characterization of the stop bands[36,39,52] in zero-order transmission and reflectivity spectra. These stop bands are typically inhomogeneously broadened, thus seriously complicating the determination of the band structure. In disordered materials overlap between stop bands measured along different directions (the usual definition of the complete PBG) may arise due to inhomogeneous broadening effects[36] in cases where a complete gap is prohibited by the limited refractive index contrast. In some cases this problem can be overcome by applying extremely high spatial resolution, so-called single domain spectroscopy,[39] allowing homogeneous linewidths in the reflectivity spectra to be approached.

More directly disorder-induced properties of self-assembled materials have been addressed in experiments with built-in sources of light,[53] total transmission,[52] and coherent backscattering.[54,55] It was found that the propagation of light generated by the built-in sources arises from a combination of *ballistic* transport (along directions away from the stop band) together with *diffuse* scattering in the thin near-surface region. However the spatial and spectral characteristics of scattered light, as well as the role of polycrystallinity, were not studied in detail in these papers.

The present paper is devoted to a systematic study of the interplay of properties determined by order and disorder in the vicinity of optical stop bands in opals obtained by standard sedimentation methods. Although they are polycrystalline, the samples selected for this work were the least disordered available to us, according to the following criteria: (i) domains are of significant size (50–100 μm), (ii) the lattices of individual domains are well ordered, (iii) the domains have narrowly defined (10° at most) preferential ori-

entation, and (iv) the distribution of the domain sizes and orientations is uniform not only along the sedimentation plane but also through the entire thickness of the sample. Generally speaking we selected samples comprising the best properties of Bragg reflectivity (narrow stop bands from individual domains) with scattering properties due to the polycrystalline structure, which is uniformly distributed through the volume of the sample. We believe that these samples are typical of most opal samples studied worldwide and that the optical properties studied in this work are general for these materials.

To access properties determined by the ensemble of a large number of domains (typically 10^3–10^4 in our experiments) we studied opals infiltrated with liquids with a relatively small contrast of refractive index. We developed experimental approaches that permit angle-resolved spectral measurements of light scattered and diffracted in all directions in space (4π-sr solid angle). We show that in the vicinity of the stop band not only the transmitted zero-order beam, but also the scattered light experience strong variations of intensity and contribute markedly to the total photon flux. We show that the shape of the stop band features in different types of optical spectra (diffraction, transmission, and scattering) is interlinked and must be studied jointly to obtain a comprehensive understanding of the optical phenomena in these materials.

We studied several effects arising from the interplay between order and disorder: (i) angular dispersion in diffraction spectra caused by slight misorientation of domains, (ii) inhomogeneous broadening of the stop band in transmission spectra, and (iii) resonant enhancement of scattering behind the sample of magnitude ∼10 times greater than the background level. It is shown that the mechanism of resonant enhancement is determined by multiple incoherent backward/forward reflections from the microcrystallites, leading to enhanced residence times of photons within the scattering medium, combined with the superprism effect in individual microcrystallites.[56,57] It is shown that the spatial pattern and form of the scattering spectra can be deduced from analysis of the set of angle-dependent zero-order transmission spectra given the condition that the attenuation length of light within the stop band is comparable with the thickness of the sample for both transmitted and scattered waves.

The paper is organized as follows. Section II describes the structure of our polycrystalline samples. In Sec. III we describe the experimental geometry. Section IV contains general remarks about optical transport in opals. Section V is devoted to diffraction properties in front of the samples. Section VI describes mechanisms leading to stop band broadening in the zero-order transmission. Section VII is devoted to scattering behind the sample. Finally, the main conclusions are summarized in Sec. VIII.

II. POLYCRYSTALLINE STRUCTURE OF SAMPLES

The samples used in these studies were manufactured by sedimentation of silica spheres in gravity followed by sintering in the temperature range 800 °C–950 °C to provide self-supporting properties of the sediment due to slight mutual

penetration and fusing of spheres (see details of fabrication in Ref. 36). The mean diameter of the silica spheres varied in different monodisperse suspensions within the range 200–400 nm. The growth of the samples took place in cuvettes ($\sim$10 cm diameter) with a rate of crystallization $\sim 10^{-7}$ cm/s. Obtaining samples with the thickness in the centimeter range typically requires from one to three months or even longer for the smallest spheres. Similar techniques have been employed by many groups[1–6] to obtain bulk samples of synthetic opals (for a review of fabrication techniques, see Ref. 58).

Such sedimentation techniques result in polycrystalline domains of varying sizes, usually with face-centered-cubic (fcc) packing or random stacking of hexagonally close-packed planes.[36,38,39] Polycrystalline structure was found in all the centimeter size samples obtained from different manufacturers.[59–61] The average size, crystal quality, and distribution of domain orientations were found to be dependent on the polydispersity of spheres, velocity of sedimentation, concentration of the suspension, charging effects, flatness of the substrate, and other features of the technological process. By using a scanning electron microscopy (SEM) analysis and optical characterization of samples polished at different depths from the top surface of the sediment we found the following major trends in the characteristics of the domain structure.

(i) The size of the domains tends to increase towards the top surface of the sediment. This property is, however, sample dependent. It can be explained by further size separation[36,37] of the spheres in the course of slow sedimentation due to the fact that lowest layers are composed of spheres with larger diameter than the upper layers. For this work we selected samples obtained from the supplier[59] where relatively uniform distribution of the domain sizes (typically in the 50–100-μm range) and orientations preserved over millimeter depths from the top surface were found.

(ii) The domains tend to have a highly ordered system of (111) planes of the fcc lattice parallel to the surface of the structure. This property, however, was found to vary depending on the manufacturer. It is interesting to note that in opals fabricated for jewelry[61] we found significantly larger domains reaching sizes $\sim$1 mm with a very broad range of orientations. This combination of properties is responsible for the best ''play of colors'' mimicking the properties of natural[7] gem opals. For the present work, however, we selected opals[59] possessing a relatively narrow distribution (10°) of the domain (111) planes around the sedimentation plane. It should be noted, however, that domains with very different orientations can still be found in these samples at low concentration. This is illustrated in Fig. 1(a) where an SEM image of the polished sedimentation surface is presented. The square type of packing of spheres in the central part of the micrograph is indicative of a domain with (100) orientation at the surface, while the surrounding areas demonstrate hexagonal packing typical of (111) orientation.

(iii) The domains usually have an irregular shape elongated parallel to the surface of the structure. In the samples selected for this work the average lateral size of domains is
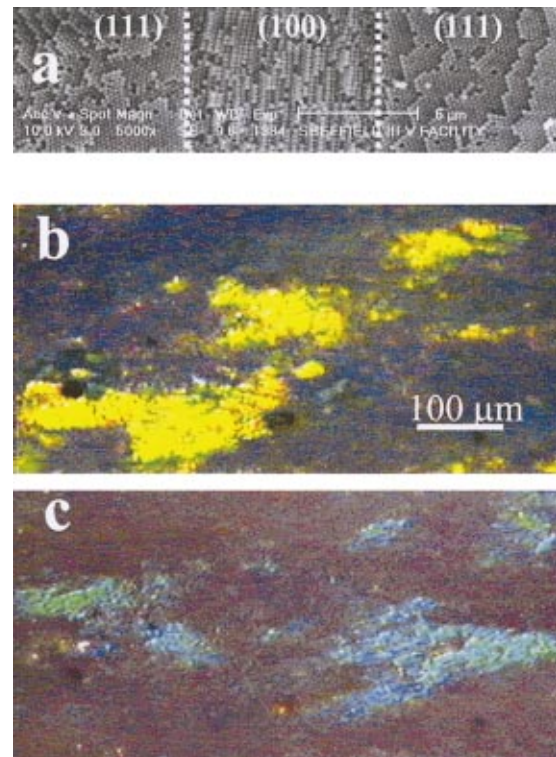

FIG. 1. (Color) (a) Scanning electron micrograph of the polished surface (parallel to the sedimentation plane) of a self-assembled opal. The square type of packing of spheres in the central part of the micrograph is indicative of a domain with (100) orientation, while the hexagonal packing in the surrounding areas represents domains with (111) planes. The dashed vertical lines represent domain boundaries. (b) (Color) Optical micrograph at a normal incidence and (c) at oblique illumination ($\theta=40°$) of the same area on the surface of the sample. The yellow and blue areas represent domains with different orientations of highly reflective (111) planes.

found to be $\sim$50–100 μm, while their average thickness was estimated to be about $\sim$10–20 μm, as discussed in Sec. V.

The samples for optical studies were obtained by cutting the sintered sedimented chunks of opals with a diamond wheel saw into a number of plates with a base surface parallel to the top surface of the sediment. To avoid faulted structures occurring near the walls of the cuvette[36] only the central part of the plates was used for fabrication of samples with lateral dimensions in the millimeter range. The samples were then polished to various thicknesses (D) spanning from 30 to 1000 μm. To provide a gradual variation of the thickness, along with the use of a number of parallelepiped-shaped samples with various thicknesses D, we also used samples polished in the form of a wedge with an angle $\sim$0.05 rad, and a base parallel to the sedimentation plane. In the optical experiments the thickness can be controlled by exact positioning of these samples relative to a small (typically $\sim$50 μm) fixed diaphragm.[4]

The main effects observed in this work are illustrated by using a single plane-parallel sample with the thickness $D = 300$ μm and size of spheres 285 nm. The advantage of this approach is that all types of spectra (transmission, diffraction, and scattering) are obtained from the same area ($\sim$3

mm^2) of the same sample, thus simplifying a comparative analysis of the results. It is necessary to note, however, that these results are very *general* and *typical* for a large number of samples with various thicknesses and sizes of spheres. We address the thickness dependence where appropriate in Secs. IV and VII. We do not discuss the dependence on the size of the spheres since we found that it is very straightforward: the shape of the band-gap features in the spectra remains similar while the energy position follows the well-known scaling of the band structures with the reciprocal of the lattice period.

The domains with different orientation can be seen directly in an optical microscope due to their bright Bragg reflectivity, as shown in Figs. 1(b) and 1(c). At different angles of illumination we observe domains with the appropriate orientation of a highly reflective (111) system of planes at the specular condition (see areas of the sample displaying different colors at normal [Fig. 1(b)] and oblique [Fig. 1(c)] incidences). The system of (111) planes possesses strongest reflectivity because of its maximal structure factor[41,62] in light scattering. The separation of strongly scattering (111) planes is robust to the presence of plane stacking faults,[36] thus leading to well-defined stop bands along this direction. In the case of broad area illumination the individual reflections from a number of rotated microcrystallites determine the pattern of diffraction in the front of the sample considered further in Sec. V.

The boundaries between individual domains [see Fig. 1(a)] are mostly imperfect areas of the polycrystalline samples and give rise to incoherent scattering of light. The scattering occurs due to refraction/reflection at the interfaces between microcrystallites of irregular shape. In addition each domain contains a finite concentration of point defects such as vacancies and interstitial spheres (typically $\sim 10^7$ cm^{-2}, or one defect per 100 unit cells) as well as dislocations and stacking faults. All these types of volume defects along with the standard 3%–5% variations of the size and index of spheres contribute to incoherent scattering of light behind the sample considered in Sec. VII.

III. EXPERIMENTAL GEOMETRY

Highly collimated (divergence $<1°$) white light illumination was provided from a tungsten-halogen lamp at an angle of incidence θ, as shown in Fig. 2. In some experiments described in Sec. VII a tunable dye laser was used as a source of light. The size of the incident beam on the sample was about 2 mm, meaning that the number of illuminated domains was of order 10^3–10^4. Light was collected in any desired direction with 1° angular resolution by use of a flexible fiber coupled to a spectrometer. The spatial pattern of light around the sample could also be observed on a removable cylindrical screen as shown schematically in Fig. 2.

In the absence of absorption, which is typically a very good approximation in our experimental conditions, the balance of beams originating from the slab of opal can be represented as

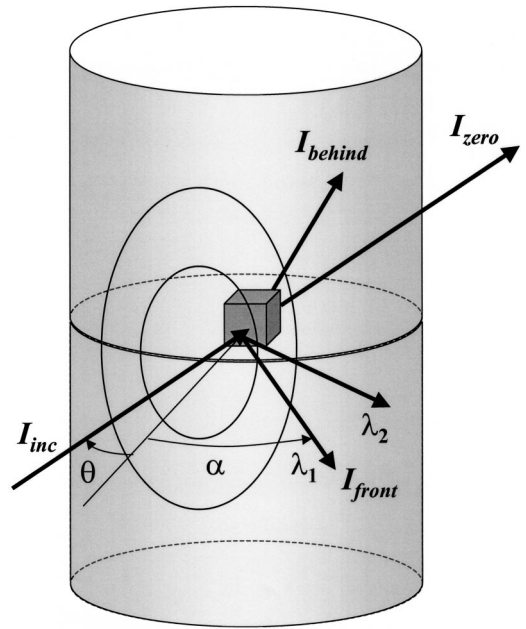$$I_{\text{inc}} = \Sigma I_{\text{front}} + I_{\text{zero}} + \Sigma I_{\text{behind}}, \qquad (1)$$

FIG. 2. Schematic representation of the geometry of the experiment with incidence (I_{inc}) provided at angle θ and the diffracted and scattered light visualized on a cylindrical screen. The pattern of diffraction in front of the sample (I_{front}) expected for a Debye-Scherrer mechanism is represented by ellipses concentric with I_{inc}. The beams λ_1 and λ_2 represent a small part of the concentric ellipses along various angles α observed in the plane of incidence. The beams I_{zero} and I_{behind} represent the zero-order transmitted beam and scattered light behind the sample, respectively.

where I_{inc} is the intensity of the incident beam, ΣI_{front} the integrated intensity of the beams diffracted and scattered in front of the sample (2π-sr solid angle), I_{zero} the intensity of the zero-order transmitted beam measured along the line-of-sight direction behind the sample, and ΣI_{behind} the total intensity of light behind the sample (2π-sr solid angle), excluding I_{zero}. More details on the experimental geometry can be found in the following sections.

We will show that in the vicinity of the stop band both diffraction and scattering are resonantly enhanced and all terms in Eq. (1) display a complex interplay as a function of energy. For this reason all types of spectra of these materials must be studied jointly to obtain a reliable understanding of the optical properties.

IV. GENERAL REMARKS ABOUT OPTICAL TRANSPORT

A. Incoherent scattering and Bragg reflectivity

For photons with energies far from the optical stop band, the optical transport through the slab of opal can be characterized by a mean free path for photons (l) determined by incoherent scattering of light on various defects in the structure. The dried as-grown opals have a milky appearance in a broad range of wavelengths because of the small values of the parameter l (~ 15–20 μm),[52–55] leading to strong attenuation of the total transmission ($T = I_{\text{zero}} + \Sigma I_{\text{behind}}$) in the classical diffusion limit ($l \ll D$): $T = 1/D$. The parameter l is
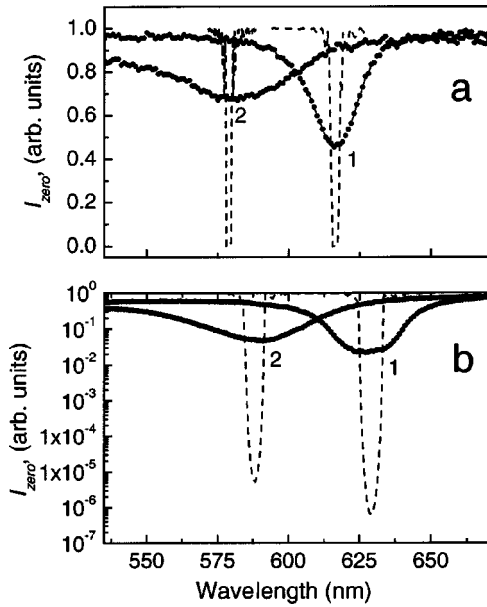
FIG. 3. Experimental (solid lines) and theoretical (dashed lines) zero-order transmission spectra (a) for infiltration with ethanol and (b) with cyclohexane. The spectra marked 1 represent normal incidence ($\theta=0°$), while the spectra marked 2 show the case of incidence at $\theta=30°$. The calculations predict significantly stronger attenuation and narrower spectral width of the stop band features even though in the calculations the thickness of the structure was smaller [90 μm, corresponding to 384 close-packed (111) layers with interplane spacing of $d=233$ nm] than the actual thickness of the sample ($D=300$ μm).

controlled by the index difference between spheres ($n_s = 1.33$) (Ref. 63) and pores (n_p). In dried opals the refractive index contrast ($\Delta n/n$, where $\Delta n = n_s - n_p$, and n is the average index) reaches ~0.3, thus leading to small values of the parameter l.

To reduce scattering and to probe the whole thickness of the sample ($l \geqslant D$) in our experiments the pores were infiltrated with ethanol with a refractive index $n_p = 1.36$ or with cyclohexane with an index $n_p = 1.43$. The infiltration was performed in an optical cuvette with flat walls. Zero-order transmission measurements demonstrate that after infiltration the samples are much more transparent ($I_{zero} \geqslant \Sigma I_{front} + \Sigma I_{behind}$) in a broad range of wavelengths, except for the stop band region, as shown in Fig. 3(a) for ethanol and in Fig. 3(b) for cyclohexane.

At the stop band energies the zero-order beam is exponentially attenuated with the thickness of the sample[2,4] [$I_{zero} \sim \exp(-D/L_{exp})$, where I_{exp} is the measured attenuation length] due to Bragg reflectivity, which leads to the pronounced dip in Fig. 3. The value of L_{exp} was found to be 300 and 60 μm in the cases of infiltration with ethanol and cyclohexane, respectively. This was confirmed by additional measurements of the transmission thickness dependence performed on the wedge-shaped sample.[4] The dip shifts markedly to shorter wavelengths with an angle of incidence θ, as seen in the transmission data for $\theta=0°$ and at $\theta=30°$ in Fig. 3. In the case of infiltration with ethanol the attenuation of the zero-order beam [~50% I_{inc}, see Fig. 3(a)] was found to

TABLE I. Parameters of optical transport: l is the transport mean free path, L the Bragg attenuation length calculated for the [111] direction of a perfectly ordered fcc lattice, L_{exp} the attenuation length measured in the polycrystalline sample along the direction of sedimentation, Δ the full width at half maximum (FWHM) of the stop band feature in calculated spectra, and Δ_{exp} the experimental FWHM of the stop band.

Liquid	n_p	Contrast	l	L (μm)	L_{exp} (μm)	Δ (nm)	Δ_{exp} (nm)
Ethanol	1.36	-0.022	$\gg$D	40	300	3	18
Cyclohexane	1.43	-0.073	$\sim$D	12	60	9	~50

be mainly due to Bragg diffraction of light in front of the sample ($I_{zero} \sim \Sigma I_{front} > \Sigma I_{behind}$). However, in the case of cyclohexane the intensity of the zero-order beam drops to $\sim 10^{-2} I_{inc}$ at the midgap frequencies [see Fig. 3(b)]. As shown in Sec. VI for these conditions the intensity of the light scattered behind the sample exceeds the intensity of the zero-order beam ($\Sigma I_{behind} > I_{zero}$), and represents a significant contribution to the total balance of photons.

B. Failure of the perfect lattice model

Attempts to describe the transmission properties within the approximation of a perfectly periodic system lead to serious disagreement with the experimental spectra, as found from one-dimensional[52] modeling and as shown below from three-dimensional[64,65] (3D) calculations for the fcc lattice.

The results of 3D calculations for incidence on a system of (111) planes are represented by dashed lines, for direct comparison with experiment, for the cases of infiltration with ethanol [Fig. 3(a)] and cyclohexane [Fig. 3(b)] at two angles of incidence $\theta=0°$ and $\theta=30°$. It is seen that although the calculations correctly describe the positions of the centers of the experimentally observed dips and their angular shift, they predict significantly stronger attenuation in the gap and narrower spectral width of the stop band features. The difference between the calculated parameters (Bragg attenuation length of light at midgap L and linewidth of the stop band Δ) and corresponding parameters determined from the experimental spectra (L_{exp} and Δ_{exp}) is striking. These parameters are given in Table I for the cases of infiltration with ethanol and cyclohexane. It is seen that $\Delta_{exp}/\Delta \sim 6$, demonstrating the very strong inhomogeneous broadening of the experimental spectra. The experimentally measured attenuation length of light is found to be several times longer than that in the calculations. The failure of the perfect lattice model is indicative of the more complicated optical transport which occurs in a polycrystalline material.

V. DIFFRACTION IN FRONT OF SAMPLE

Study of the spatial patterns and spectral properties of light in front of the illuminated surface I_{front} allows access to specific properties determined by the polycrystalline structure. In this section we will concentrate on the resonant properties determined by the bulk properties of microcrystallites
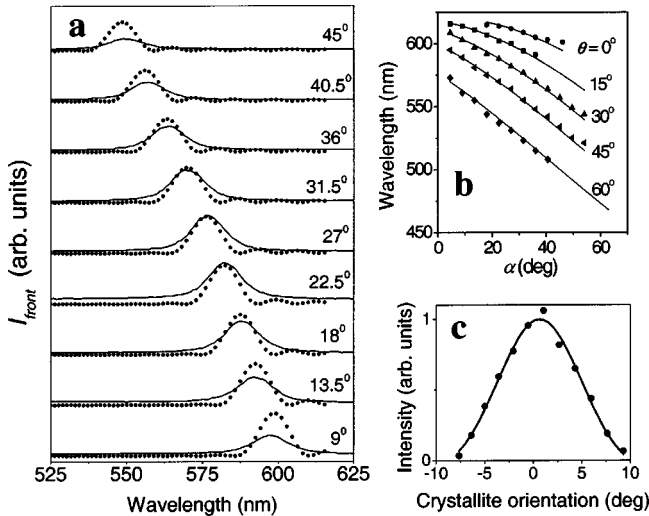
FIG. 4. (a) Experimental angle-resolved spectra (full lines) for $\theta=30°$ and α varying from 9° to 45° compared with theoretical reflectivity spectra for fcc structures with $n_p=1.36$ and $n_s=1.33$ (dotted lines). In the calculations, the structure has a thickness of 90 μm corresponding to 384 close-packed (111) layers with interplane spacing of $d=233$ nm. The measured peak intensities are normalized to fit the calculated spectra at the specular condition $\alpha=\theta=30°$. (b) Measured angular dispersion of the center of the stop bands for $\theta=0°$, 15°, 30°, 45°, and 60° as a function of α (symbols), and calculated using Eqs. (2) and (3) (full lines). (c) Measured intensity of the peak as a function of rotation of (111) planes relative to the plane of sedimentation (symbols), and Gaussian fit (full line).

(Bragg reflectivity) (Ref. 66) rather than on the incoherent scattering from boundaries between domain and from various structural imperfections. The pattern of I_{front} has a close analogy with the case of x-ray diffraction in powders[67] with one important difference. In powders all orientations of microcrystallites are equally represented. For this reason Bragg diffraction is typically observed for all rays along the generators of cones concentric with the beam incident on the sample. These cones should intercept the cylindrical screen around the sample in a series of concentric ellipses corresponding to different wavelengths, as shown in the schematic sketch of Fig. 2. However, in synthetic opals the system of (111) planes has a strong preferential orientation along the surface, thus allowing only a small part of the concentric ellipses along various angles α in the plane of incidence to be observed, as represented by the beams λ_1 and λ_2 in Fig. 2.

Angle-resolved diffraction spectra measured at different angles α (for fixed θ of 30°) in the plane of incidence are presented in Fig. 4(a) for the case of infiltration with ethanol. The diffraction peaks have width ~13 nm for all α, peaking in intensity at the specular condition $\alpha=\theta=30°$, and with the peak wavelength decreasing with increasing α, similar to previous observations[24,36] performed at higher refractive index contrasts.

The results can be modeled in the low index contrast limit by considering Bragg's law (2), along with Snell's law to describe refraction at the flat wall of the cuvette, with the

average index $n=[(n_s)^2 f+(n_p)^2(1-f)]^{1/2}$, where $f=0.74$ is the filling factor for the close-packed fcc structure. The dispersion relation can be obtained by assuming that for each combination of external angles α and θ we selectively probe the reflectivity of the appropriately oriented domains [at the specular condition represented by an internal angle φ of incidence on the system of (111) planes]:

$$m\lambda = 2nd \cos\varphi, \qquad (2)$$

$$\varphi = \frac{1}{2}\left[\arcsin\left(\frac{\sin\theta}{n}\right)+\arcsin\left(\frac{\sin\alpha}{n}\right)\right], \qquad (3)$$

where $m=1$ is the diffraction order and $d=0.816a$ is the separation between (111) planes.

This model very well describes the angular dispersions of the positions of the peaks in the diffraction spectra[68] for a very broad range of angles α and θ varying from 0° to 60°, as shown in Fig. 4(b). This is further confirmed by our calculations of reflectivity spectra from a series of perfectly ordered fcc lattices using a 3D code,[64,65] each lattice slightly rotated to represent *specular* incidence at angle φ for each combination of α and θ. In the calculations the size of the lattice along the (111) plane was assumed to be infinitely large, consistent with the large lateral dimensions (50–100 μm) of the domains. The thickness of the lattice along the propagation direction was treated as a fitting parameter with the best results obtained within the 10–20 μm range. Good agreement with the experiments for both the width and position of the diffraction lines was obtained, as shown by the dotted lines in Fig. 4(a) for thickness 11.2 μm. For thicker material (up to 100 μm) the calculations show narrowing of the stop band, roughly by a factor of 2, together with the development of a square top to the reflection peak (indicative of close to 100% absolute reflectance), which is not seen in the experiments. The good agreement obtained for the smaller thicknesses indicates a lower limit to the domain thicknesses ($D_{dom}\sim10$ μm) in our samples.

The distribution of the domain orientations can be studied by comparing the intensities of the calculated and measured diffraction peaks in Fig. 4(a). The intensities of the experimental peaks are normalized to fit the calculated spectra at the specular condition $\alpha=\theta=30°$. The intensities decrease rapidly for smaller and larger α showing the preferential orientation of domains around the [111] growth direction. From the variation of the diffracted intensity with α away from 30°, we deduce an approximately Gaussian distribution of orientation of (111) planes with full width at half maximum (FWHM) of 10° as shown in Fig. 4(c).

VI. BROADENING EFFECTS IN ZERO-ORDER TRANSMISSION SPECTRA

The broadening of the stop band reported in Sec. IV is too large[52] to be explained by the standard deviation (3%–5%) of the sphere sizes. In this section we will show that this effect arises from the polycrystalline nature of synthetic opals. The full picture is, however, complicated by the occurrence of the three distinctly different mechanisms considered below. The first two mechanisms take place in the limit
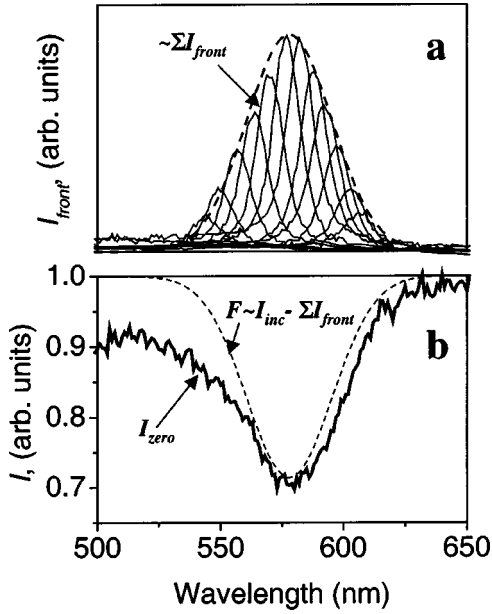
FIG. 5. (a) Experimental diffraction peaks for $\theta=30°$ in the case of infiltration with ethanol [same as in Fig. 4(a)] represented without vertical shift (full lines). The envelope function (dashed line) represents the spectral shape of the term ΣI_{front} in the balance Eq. (1). (b) Experimental zero-order transmission spectrum I_{zero} in ethanol at $\theta=30°$ (full line) and the function $F=I_{\text{inc}}-\Sigma I_{\text{front}}$ (dashed line). The function F is normalized for direct comparison with I_{zero}.

of weak refractive index contrast. They are illustrated by the case of infiltration with ethanol. The third mechanism is revealed in experiments with larger contrasts, the case of infiltration with cyclohexane.

(i) *Homogeneous broadening* caused by the finite thickness of the individual domain in the limit $(D_{\text{dom}}\lesssim L)$ has been previously studied[32] in opal thin films. It can be seen from a comparison of the theoretical curves in Figs. 3(a) and 4(a): the diffraction peaks calculated for $D=11.2$ μm are broader (FWHM$\sim$10 nm) than the features in transmission[69] (FWHM$\sim$3 nm) calculated for thicker material $D=90$ μm.

(ii) *Inhomogeneous broadening*, due to the fact that the total intensity of light rejected from the zero-order beam at the stop band frequencies, arises from a number of individual diffraction peaks[70] with different wavelengths from different domains. This mechanism of broadening is illustrated in Fig. 5(a) where the diffraction peaks measured for different α at $\theta=30°$ [see Fig. 4(a)] are combined on a single plot. The envelope (dashed curve) displays a peak inhomogeneously broadened (FWHM$\sim$40 μm) by comparison with the individual lines (FWHM$\sim$13 nm). This peak represents the spectral shape of the term ΣI_{front} in Eq. (1). Its position, width, and strength very well fit the shape of the dip observed in the transmission spectrum[71] at $\theta=30°$, as shown in Fig. 5(b). This agreement indicates that the relationship $I_{\text{zero}}=I_{\text{inc}}-\Sigma I_{\text{front}}$ is roughly satisfied, showing that the scattering term does not play a significant role $(\Sigma I_{\text{behind}}\ll I_{\text{zero}})$ in the total balance of photons represented by Eq. (1). This conclusion was additionally proved by direct measurements of the scattered intensity behind the sample $(\Sigma I_{\text{behind}})$, which showed that this term constitutes only a few percent of I_{zero} at all
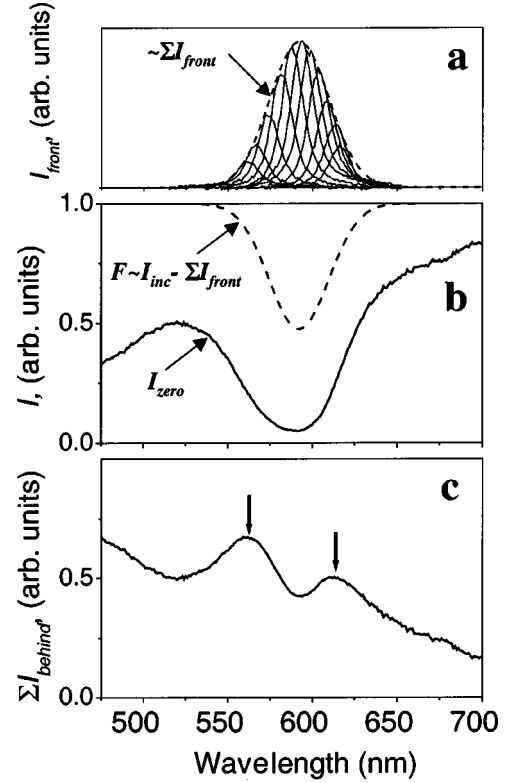

FIG. 6. (a) Experimental diffraction peaks for $\theta=30°$ in the case of infiltration with cyclohexane at different angles α from 9° to 45° (full lines). The envelope function (dashed lines) represents the spectral shape of the term ΣI_{front} in the balance Eq. (1). (b) Experimental zero-order transmission spectrum I_{zero} in cyclohexane at $\theta=30°$ (full line) and function $F=I_{\text{inc}}-\Sigma I_{\text{front}}$ (dashed line). (c) The spectral shape of the angle-integrated scattering behind the sample, as deduced from $\Sigma I_{\text{behind}}=F-I_{\text{zero}}$. The two marked peaks indicate resonant enhancement of scattering at the stop band edges.

frequencies. Thus coherent Bragg diffraction by the polycrystalline structure $(\Sigma I_{\text{front}})$ is the dominant factor leading to the shape of the stop band in the case of infiltration with ethanol.

(iii) *Additional broadening* due to incoherent scattering arises when for larger index contrasts (cyclohexane) mechanism (ii) is insufficient to describe the shape of the stop band features in zero-order transmission. This is illustrated in Fig. 6 where a similar treatment of the diffraction data to that of Fig. 5 for different α at $\theta=30°$ leads to an envelope function of individual peaks with a linewidth (FWHM$\sim$40 nm) very similar to the case of ethanol [Fig. 6(a)]. However, as seen in Fig. 6(b), this envelope function cannot explain key features of the transmission spectrum including the much broader dip as well as the shape of the background, which displays a marked decrease towards shorter wavelengths. The difference between $F\sim I_{\text{inc}}-\Sigma I_{\text{front}}$ and I_{zero} in Fig. 6(b) arises from scattering behind the sample[72] $(\Sigma I_{\text{behind}})$ [see Eq. (1)]. The spectral shape of the term ΣI_{behind} found by this procedure is represented in Fig. 6(c). It is seen that the scattering term ΣI_{behind} has a magnitude comparable with I_{zero} in the whole range of wavelengths, except at the stop band frequencies where ΣI_{behind} completely dominates I_{zero}. Most inter-

estingly, the term ΣI_{behind} is *resonantly enhanced* at the stop band edges as indicated by the two marked peaks in Fig. 6(c). This effect is responsible for the additional broadening of the stop band in the zero-order transmission spectra.

VII. SCATTERING BEHIND THE SAMPLE

To provide direct evidence for the occurrence of scattering and to study its role in determining the overall optical properties, we performed measurements of scattering spectra with angular resolution. We begin with the results obtained in the case of infiltration with ethanol where $L_{\text{exp}} = D = 300$ μm. These results were found to be qualitatively similar to those obtained using various ethanol-methanol mixtures (index between 1.33 and 1.36) with smaller refractive index contrasts (between 0 and -0.022) where $L_{\text{exp}} > D$. Thus the infiltration with ethanol was chosen as a case fully representative of the regime of weak Bragg attenuation ($L_{\text{exp}} \gtrsim D$). We will interpret these results and discuss a model for scattering in polycrystalline opals. Finally, we consider additional experiments for larger index contrasts (cyclohexane) that provide additional support to our model. They will be discussed along with the thickness dependence of the scattering spectra.
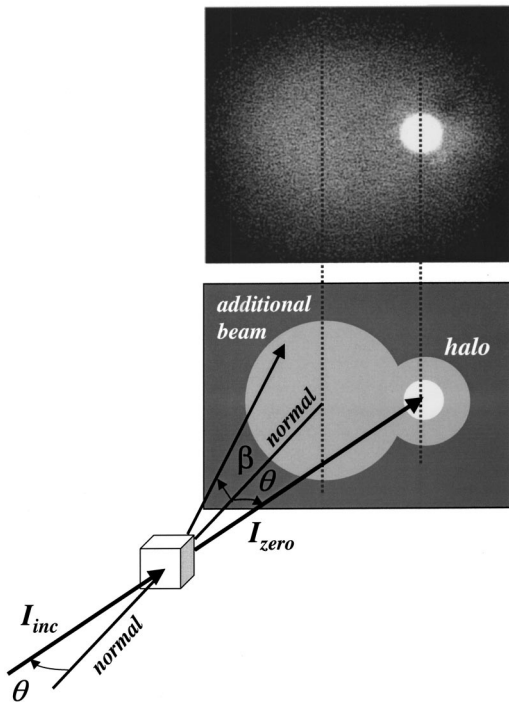

FIG. 7. Pattern of scattered light behind the sample observed in the case of illumination at $\theta = 20°$ by a tunable dye laser of wavelength 618 nm in the stop band region. The resonantly enhanced scattering manifests itself as an additional beam, shown for clarity in the schematic sketch. It is scattered in a broad cone of directions represented by the polar angle β (from the normal). The white circle represents the zero-order transmitted beam surrounded by a diffuse halo.

A. Scattering in the regime of weak Bragg attenuation (ethanol)

Although infiltration with ethanol leads to a weak intensity of scattering (ΣI_{behind}) compared to other terms in Eq. (1), this case is fully representative of the scattering properties of opals observed in this paper and is very helpful in revealing the physical mechanisms. Our main observations are that the scattering is *resonantly enhanced* at the stop band energies, and in addition gives rise to an additional beam of light behind the sample, as shown in Fig. 7. This beam has properties very different from conventional scattering, which gives rise to the diffuse halo surrounding the zero-order transmitted beam, also visible in Fig. 7. The additional beam appears only at the stop band energies (the image in Fig. 7 is obtained for a single wavelength within the stop band), while the diffuse halo occurs for a wide range of wavelengths. The additional beam is characterized by a broad cone of directions, centered around the normal to the sample as given by the polar angle (β), as shown in Fig. 7.[73] In contrast, the diffuse halo is scattered in a much narrower cone around the zero-order beam.

The spectral properties of the scattered light are presented in Fig. 8(a) for the case of normal incidence ($\theta = 0$) when both beams (diffuse halo and additional beam) are centered around the same direction ($\beta = \theta = 0$), but with different angular widths (Fig. 7). The spectra measured at different angles β exhibit a peak due to the additional beam and an almost wavelength-independent background from the diffuse halo. The amplitude of the peak is comparable with the background for small β. For increasing β, the background decays rapidly and the peak overtakes the level of the background by at least an order of magnitude, as seen in spectrum 2 of Fig. 8(a). This arises due to the broader directionality of the additional beam compared with that of the diffuse halo. The position (620 nm) and width (FWHM $\sim$10 nm) of the peak at small β correlate with that of the stop band in the zero-order transmission spectra at $\theta = 0$, as seen by comparison with Fig.
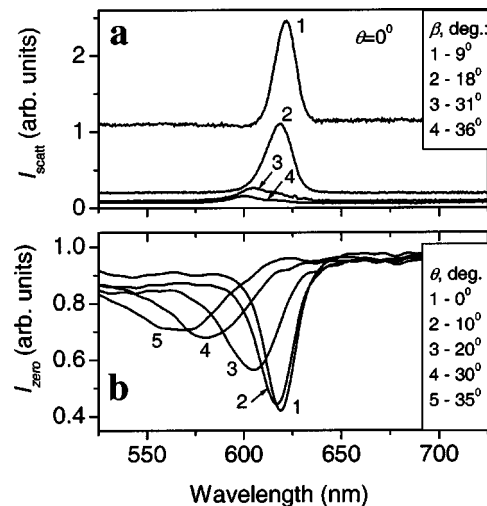

FIG. 8. (a) Experimental scattering spectra for normal incidence ($\theta = 0°$) and various scattering angles β from 9° to 36° in the case of infiltration with ethanol. (b) Zero-order transmission spectra for various angles of incidence θ from 0° to 35° in the case of ethanol.

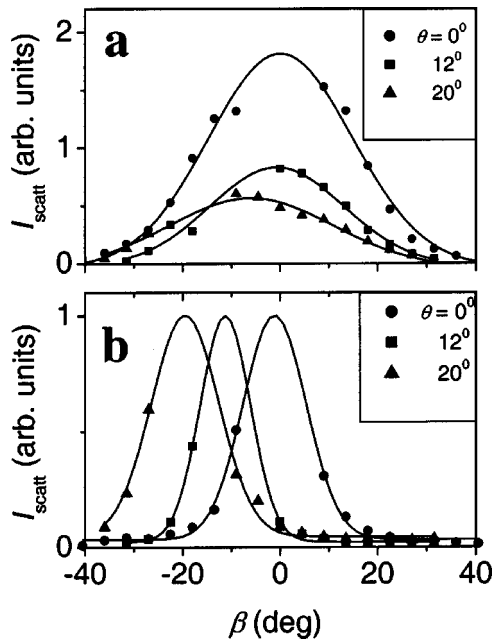FIG. 9. Measured angular (β) distributions of the peak (a) and background (b) in the scattering spectra (symbols). The amplitude of the peak was measured from the level of the background for $\theta=0°$, 12°, and 20°. The position of the peak (a) is varying between 600 and 625 nm for different θ and β [see β dependence for $\theta=0°$ in Fig. 8(a)]. The level of the background (b) was measured at 650 nm (the results are, however, independent of the wavelength apart from the region 600–626 nm because of the flat shape of the background). The solid lines represent a Gaussian fit to the experimental data.

8(b). As the angle β increases the peak displays a slight shift to shorter wavelengths accompanied by weakening and broadening. It is important to stress that the shift of the peak as a function of angle β is very weak compared to the shift of the stop band in the zero-order transmission measured for $\theta=\beta$ in Fig. 8(b).

The directionality of scattering for the peak (additional beam) and the background (diffuse halo) are shown in Figs. 9(a) and 9(b), respectively. The measurements were performed for different θ as a function of detection angle β, as shown in Fig. 7. The amplitude of the peak was measured from the level of the background. It is seen that for each θ the scattering peak occurs over a very *broad* range of angles β with angular widths as large as $\sim 40°$, centered either at ($\theta < 15°$) or close to ($\theta > 15°$) the normal direction. In contrast the background scattering has *narrow* directionality of $\sim 15°$ with the direction of maximum intensity (β_m) occurring along the direction of illumination, $\beta_m = -\theta$, as illustrated in Fig. 9(b).

B. Interpretation of the results and discussion of the model

The diffuse scattering halo around the zero-order beam is well known from previous studies of opals,[36] and arises from scattering by structural defects. The fact that its spectrum is wavelength independent[74] shows that it arises from scattering (refraction and reflection) by particles, of irregular shape,

large compared to a wavelength,[75,76] rather than from diffraction or scattering by features with sizes on a wavelength scale. In our samples, domains with irregular shape and very large size (50–100 μm) probably play the role of the large particles. The direction of the halo (which follows the direction of illumination) is explained by the fact that the medium is almost transparent $I_{zero} \sim 0.9 I_{inc}$ and thus the initial direction of propagation (dictated by the zero-order beam) is only weakly perturbed upon propagation through the entire thickness of the material. The relatively narrow directionality of the scattering ($\sim 15°$) also arises from the high transparency of the material due to low refractive index contrast.

The additional beam, resonantly peaked at the stop band and centered either at or close to the normal depending on the angle of incidence, has a totally different origin from that of the background. At first sight the spectral enhancement at or close to the $\theta=0$ stop band energy is particularly surprising, since suppression rather than enhancement might have been expected at this energy and along the direction with the maximum Bragg effect (the $\langle 111 \rangle$ average direction). The observation can, however, be understood if we take into account some specific features of light propagation through the system of slightly misoriented crystallites.

At the resonant Bragg condition each microcrystallite is strongly reflective in the limit $L \sim D_{dom}$. This transforms the propagation path into a series of forward/backward reflections between different domains. As a result light spends a longer time within the medium (due to the zigzag propagation between the domains). This resonantly increases the probability of scattering as well as leading to a spread in the cone of scattered light: after a few scattering events, the initial direction (dictated by the zero-order beam) is "forgotten," and the angular distribution of scattered light fills the entire distribution of the misorientations of the domains irrespective of the direction of incidence. This effect of resonant "dwelling" of light within the polycrystalline structure also explains why the additional beam is symmetric about the normal direction, independent of the incidence angle.

An additional factor that may also contribute to the broad directionality of the scattered light (additional beam) is connected with the superprism effect,[56,57] which leads to larger angles of refraction within each domain at band-edge frequencies. Although quantitative analysis is complicated by the polycrystalline structure of the samples calculations performed for a single crystal predicted[57] dramatic increases of the refraction angles in the vicinity of the optical stop band.

It is interesting to note that the properties of the scattering spectra can be deduced from analysis of the zero-order transmission spectra measured along different directions. The optimal conditions for scattering can be represented by the following rules based on the use of the experimental parameter L_{exp} representing the attenuation length at the center of the stop band measured along different directions:

(i) The scattering behind the sample is optimized if the condition $L_{exp} \sim D$ holds for the zero-order beam since in the case $L_{exp} \gg D$ the scattering is insignificant in comparison with the intensity of the zero-order beam, while in the opposite case $L_{exp} \ll D$, light with the midgap energy is mainly

diffracted in front of the sample, with the result that there will be no scattered light behind the sample.

(ii) The overall process is optimized if not only the zero-order beam but also the light scattered in a given direction spends longer time within the medium. This means that we have effectively a double optical resonance for the scattering process with the density of initial (zero-order) and final (direction of detection) states resonantly enhanced due to multiple reflections between domains. The same condition $L_{exp} \sim D$ is expected to hold for the scattered light.

These rules allow all the major features of the scattering spectra for normal incidence ($\theta = 0$) in Fig. 8(a) to be explained. For small β the back reflection (attenuation) of the scattered light is given by the low-angle ($\theta = \beta$) zero-order transmission spectra in Fig. 8(b), which have stop bands nearly identical to that for the zero-order beam at $\theta = 0$ [compare spectra 1 and 2 in Fig. 8(b)]. The attenuation of both beams approaches the optimal condition $L_{exp} \sim D$ near midgap, thus explaining the single peak in the scattering spectra at 620 nm. For large-angle scattering ($\beta \geq 30°$), because of the angular shift and weakening of the corresponding stop band ($L_{exp} \gg D$), see Fig. 8(b), the final scattering has no enhancement specific due to the increased residence time (dwelling) of the light, so the peak amplitude weakens. In this model, the spectral position of the scattering peak is thus determined by the product of the transmission spectra for the initial and final waves (for given β): this occurs close to the intersection point of the short-wavelength edge of the normal incidence stop band and the long-wavelength edge of the stop band at $\theta = \beta$. This explains why the shift of the peak in the scattering spectra with β is very much smaller than the corresponding shift (at $\theta = \beta$) of the stop band in the zero-order transmission. The broad directionality of the scattering then arises from the fact that good overlap between the stop bands at $\theta = 0$ and $\theta = \beta$ is preserved up to angles $\beta \sim 20°$ due to the effects of inhomogeneous broadening considered in Sec. VI. For incidence away from the normal [Fig. 7, and Fig. 9(a), the triangles], the resonant scattering is still centered along the directions close to $\beta = 0$ since in the limit of weak Bragg attenuation ($L_{exp} \geq D$) we can only approach the optical conditions for scattering for both beams in the case of scattering at directions close to normal.

This mechanism is consistent with additional measurements performed on samples with smaller thicknesses (down to 30 μm) where a similar single peak was observed in the scattering spectra in the regime of weak Bragg attenuation ($L_{exp} \geq D$). For thicker samples (up to 1000 μm) where the regime of strong Bragg attenuation ($L_{exp} = 300$ μm $< D$) occurred, we observed transformation of the single peak into a two-peak structure. This regime of scattering can also be realized by using infiltration of the same reference sample ($D = 300$ μm) with cyclohexane where L_{exp} drops down to 60 μm. These results are considered in the following section.

C. Scattering in the regime of strong Bragg attenuation (cyclohexane)

Scattering spectra for infiltration with cyclohexane are shown in Fig. 10(a) for normal incidence. In the same way as
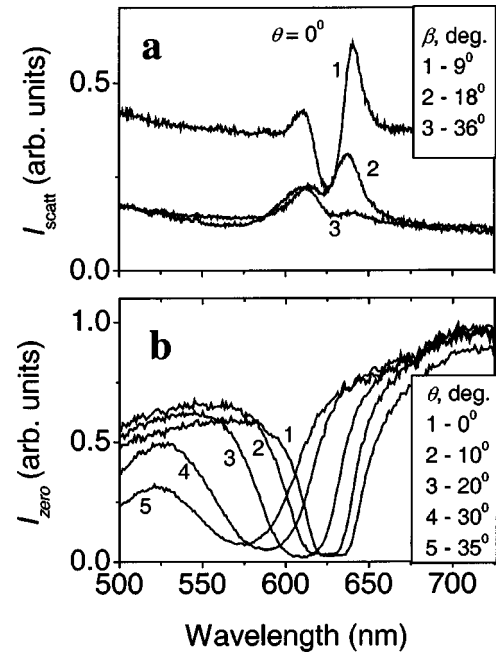

FIG. 10. (a) Experimental scattering spectra for normal incidence ($\theta = 0°$) and various scattering angles β from 9° to 36° in the case of infiltration with cyclohexane. (b) Zero-order transmission spectra for various angles of incidence θ from 0° to 35° in the case of cyclohexane.

for ethanol, the spectra display a relatively flat background due to refraction/reflection phenomena at the boundaries of "big" particles with irregular shape. The intensity of scattering is, however, stronger and the directionality of the "halo" is broader due to the larger refractive index contrast compared with ethanol.

The resonant behavior is particularly interesting since instead of a single peak, we now observe several resonant features in the stop band region. At small angles ($\beta \sim 10°$) we observe resonant enhancement of scattering at the stop band edges (peaks at 610 and 640 nm) with significant suppression of intensity at the midgap energy (dip at 625 nm), as seen by comparison with the zero-order transmission spectra in Fig. 10(b). With increase of the scattering angle up to $\beta \sim 30°$, the dip and the long-wavelength peak weaken, with the short-wavelength peak at 610 nm increasingly dominating the scattering spectra.

Integration of the scattering spectra over all β leads to overall scattering spectra with two peaks at the stop band energies similar to the spectral form of ΣI_{behind} deduced in Sec. VI from the difference between the zero-order transmission and the angular-resolved diffraction spectra shown in Fig. 6(c). The mechanism of resonant enhancement of scattering at the band edges is likely to involve both effects mentioned in the discussion of the ethanol data: (i) longer residence time of the light within the polycrystalline structure due to multiple reflections between the domains leading to enhanced scattering, and (ii) the superprism effect in the individual microcrystallites[56,57] leading to scattering at larger angles where the transmission is improved.

The shape and angular evolution of the scattering spectra in cyclohexane can be explained by analysis of the angle-dependent transmission data in Fig. 10(b), in the same way as performed for ethanol in the previous subsection. The main difference compared to the ethanol case in Fig. 8 is the very strong attenuation of the zero-order beam at the center of the normal-incidence stop band (only ~1% transmission). For this reason in the limit of small β where the stop bands for the zero-order beam and scattered waves almost coincide, the propagation lengths are very small ($L_{exp} \ll D$), and most of the incident light is reflected back out of the sample before multiple scattering can occur. However, at the edges of the stop band the optimal condition ($L_{exp} \sim D$) can be met for both initial (zero-order) and final (scattered) waves, thus explaining the two scattering peaks, separated by a dip, which are observed in the experimental spectra. The angular evolution of the scattering spectra in cyclohexane can also be understood in this way. For $\beta > 30°$ due to the strong shift of the stop band for the outgoing wave (at $\theta = \beta$), the condition $L_{exp} \sim D$ can be met for both waves simultaneously only at the short-wavelength edge of the stop band at normal incidence, leading to a single peak in large-angle scattering.

In conclusion different regimes of scattering can be controlled not only by using various liquids of differing refractive indices but also by changing the thickness of the sample. In our experiments we realized the transition from strong to weak Bragg attenuation by reducing the thickness D in the case of infiltration with cyclohexane. By using a wedge-shaped sample we found that the two-peak structure in small-angle scattering spectra (Fig. 10) gradually evolves into a single peak for sample thicknesses smaller than ~60 μm. The position of this peak was found to be well correlated with the center of the stop band at normal incidence, similar to the case of scattering in ethanol considered in Sec. VII A.

VIII. SUMMARY

The optical properties studied in this paper are determined in a fundamental way by the polycrystalline structure of the samples. The origin of the polycrystallinity is intimately related to the growth techniques of sedimented opals. These properties are extremely common for a variety of self-assembled materials including synthetic and natural precious opals, opaline thin films, and colloidal crystals. It also occurs in self-assembled materials synthesized by different approaches such as block copolymer systems and biological self-organized systems. For this reason we believe the results of this work are relevant to studies of a wide variety of materials whose properties are determined by the interplay of order and disorder effects.

In photonic crystalline optics, propagation phenomena are usually considered for plane waves coherently scattered or diffracted by the periodic structure.[77] In contrast in disordered media the propagation of light was traditionally considered as an entirely different problem of incoherent scattering[75,76] on various particles and structural imperfections. In this paper we show that in self-assembled opals due to their polycrystalline structure both mechanisms of transport coexist, and exhibit a complex interplay in the vicinity of the stop band where ballistic propagation is resonantly suppressed. We have developed a combination of experimental techniques, based on simultaneous investigation of the spatial and spectral characteristics of the diffracted and scattered light, to understand the observed phenomena. This includes angle-resolved spectroscopic measurements for all directions in space, analysis of the balance of photon fluxes, and establishing links between the shapes of the stop band features in different types of spectra (diffraction, transmission, and scattering). These techniques provide a powerful tool to characterize large areas of such materials, revealing information on the size and orientation of the domains and their photonic band structure.

The principal effects studied in this paper are (i) angular dispersion of stop bands in diffraction spectra, (ii) inhomogeneous broadening of the stop band in zero-order transmission, and (iii) effect of resonant enhancement of scattering at the stop band energies. We show that these effects are generically linked and should be observable in a wide class of self-assembled photonic crystals. The resonant enhancement of scattering in polycrystalline photonic crystals observed in this work is of interest for emission and laser applications. Due to the special type of optical feedback provided by the multiple reflections from the domains, these properties can be considered as a natural precursor for the photonic band-edge lasing in such materials.

*Author to whom correspondence should be addressed. Electronic address: astratov@uncc.edu

[1] V. N. Astratov, V. N. Bogomolov, A. A. Kaplyanskii, A. V. Prokofiev, L. A. Samoilovich, S. M. Samoilovich, and Y. A. Vlasov, Nuovo Cimento D **17**, 1349 (1995).

[2] V. N. Astratov, Y. A. Vlasov, O. Z. Karimov, A. A. Kaplyanskii, Y. G. Musikhin, N. A. Bert, V. N. Bogomolov, and A. V. Prokofiev, Phys. Lett. A **222**, 349 (1996); Superlattices Microstruct. **22**, 393 (1997).

[3] W. L. Vos, R. Sprik, A. van Blaaderen, A. Imhof, A. Lagendijk, and G. H. Wegdam, Phys. Rev. B **53**, 16 231 (1996).

[4] Y. A. Vlasov, V. N. Astratov, O. Z. Karimov, A. A. Kaplyanskii, V. N. Bogomolov, and A. V. Prokofiev, Phys. Rev. B **55**, 13 357 (1997).

[5] S. G. Romanov, N. P. Johnson, A. V. Fokin, V. Y. Butko, and C. M. Sotomayor Torres, Appl. Phys. Lett. **70**, 2091 (1997).

[6] H. Miguez, C. Lopez, F. Meseguer, A. Blanco, L. Vazquez, R. Mayoral, M. Ocana, F. Fornes, and A. Mifsud, Appl. Phys. Lett. **71**, 1148 (1997).

[7] J. V. Sanders, Nature (London) **204**, 1151 (1964); **204**, 990

(1964); **209**, 13 (1966).

[8] V. G. Balakirev, V. N. Bogomolov, V. V. Zuravlev, Y. A. Kumzerov, V. P. Petranovsky, S. G. Romanov, and L. A. Samoilovich, Crystallogr. Rep. **38**, 348 (1993).

[9] A. Blanco, C. Lopez, R. Mayoral, H. Miguez, F. Mesequer, A. Mifsud, and J. Herrero, Appl. Phys. Lett. **73**, 1781 (1998).

[10] S. G. Romanov, A. V. Fokin, and R. M. De La Rue, Appl. Phys. Lett. **74**, 1821 (1999).

[11] Y. A. Vlasov, N. Yao, and D. J. Norris, Adv. Mater. **11**, 165 (1999).

[12] A. Blanco, E. Chomski, S. Grabtchak, M. Ibisate, S. John, S. W. Leonard, C. Lopez, F. Meseguer, H. Miguez, J. P. Mondia, G. A. Ozin, O. Toader, and H. M. van Driel, Nature (London) **405**, 437 (2000).

[13] H. Miguez, E. Chomski, F. Garcia-Santamaria, M. Ibisate, S. John, C. Lopez, F. Meseguer, J. P. Mondia, G. A. Ozin, O. Toader, and H. M. van Driel, Adv. Mater. **13**, 1634 (2001).

[14] J. Wijnhoven and W. L. Vos, Science **281**, 802 (1998).

[15] M. S. Thijssen, R. Sprik, J. E. G. J. Wijnhoven, M. Megens, T. Narayanan, A. Lagendijk, and W. L. Vos, Phys. Rev. Lett. **83**, 2730 (1999).

[16] A. Richel, N. P. Johnson, and D. W. McComb, Appl. Phys. Lett. **76**, 1816 (2000).

[17] A. A. Zakhidov, R. H. Baughman, Z. Iqbal, C. Cui, I. Khairulin, S. O. Dantas, J. Marti, and V. G. Ralchenko, Science **282**, 897 (1998).

[18] K. Yoshino, Y. Shimoda, Y. Kawagishi, K. Nakayama, and M. Ozaki, Appl. Phys. Lett. **75**, 932 (1999).

[19] D. Kang, J. E. Maclennan, N. A. Clark, A. A. Zakhidov, and R. H. Baughmann, Phys. Rev. Lett. **86**, 4052 (2001).

[20] K. Yoshino, S. Tatsuhara, Y. Kawagishi, M. Ozaki, A. A. Zakhidov, and Z. V. Vardeny, Appl. Phys. Lett. **74**, 2590 (1999).

[21] M. Deutsch, Y. A. Vlasov, and D. J. Norris, Adv. Mater. **12**, 1176 (2000).

[22] K. Sumioka, H. Nagahama, and T. Tsutsui, Appl. Phys. Lett. **78**, 1328 (2001).

[23] J. Zhou, C. Q. Sun, K. Pita, Y. L. Lam, Y. Zhou, S. L. Ng, C. H. Ham, L. T. Li, and Z. L. Gui, Appl. Phys. Lett. **78**, 661 (2001).

[24] V. N. Astratov, A. M. Adawi, M. S. Skolnick, V. K. Tikhomirov, V. Lyubin, D. G. Lidzey, M. Ariu, and A. L. Reynolds, Appl. Phys. Lett. **78**, 4094 (2001).

[25] S. G. Romanov, T. Maka, C. M. Stotomayor Torres, M. Müller, and R. Zentel, Appl. Phys. Lett. **79**, 731 (2001).

[26] V. G. Golubev, V. Y. Davydov, N. F. Kartenko, D. A. Kurdyukov, A. V. Medvedev, A. B. Pevtsov, A. V. Scherbakov, and E. B. Shadrin, Appl. Phys. Lett. **79**, 2127 (2001).

[27] A. van Blaaderen, R. Ruel, and P. Wiltzius, Nature (London) **385**, 321 (1997).

[28] P. V. Braun, R. W. Zehner, C. A. White, M. K. Weldon, C. Kloc, S. S. Patel, and P. Wiltzius, Adv. Mater. **13**, 721 (2001).

[29] K. Lin, J. C. Crocker, V. Prasad, A. Schofield, D. A. Weitz, T. C. Lubensky, and A. G. Yodh, Phys. Rev. Lett. **85**, 1770 (2000).

[30] N. Denkov, O. Velev, P. Kralchevsky, I. Ivanov, H. Yoshimura, and K. Nagayama, Nature (London) **361**, 26 (1993); A. S. Dimitrov and K. Nagayama, Langmuir **12**, 1303 (1996); A. S. Dimitrov, T. Miwa, and K. Nagayama, *ibid.* **15**, 5257 (1999).

[31] P. Jiang, J. F. Bertone, K. S. Hwang, and V. L. Colvin, Chem. Mater. **11**, 2132 (1999).

[32] J. Bertone, P. Jiang, K. S. Hwang, D. M. Mittlenam, and V. L. Colvin, Phys. Rev. Lett. **83**, 300 (1999).

[33] Q.-B. Meng, Z.-Z. Gu, O. Sato, and A. Fujishima, Appl. Phys. Lett. **77**, 4313 (2000).

[34] Y.-H. Ye, F. LeBlanc, A. Hache, and Vo-Van Truong, Appl. Phys. Lett. **78**, 52 (2001).

[35] Y. A. Vlasov, X.-Z. Bo, J. C. Sturn, and D. J. Norris, Nature (London) **414**, 289 (2001).

[36] Y. A. Vlasov, V. N. Astratov, A. V. Baryshev, A. A. Kaplyanskii, O. Z. Karimov, and M. F. Limonov, Phys. Rev. E **61**, 5784 (2000).

[37] B. Cheng, P. Ni, C. Jin, Z. Li, D. Zhang, P. Dong, and X. Guo, Opt. Commun. **170**, 41 (1999).

[38] R. C. Salvarezza, L. Vazques, H. Miguez, R. Mayoral, C. Lopez, and F. Meseguer, Phys. Rev. Lett. **77**, 4572 (1996).

[39] Y. A. Vlasov, M. Deutsh, and D. J. Norris, Appl. Phys. Lett. **76**, 1627 (2000).

[40] P. N. Pusey and V. van Megen, Nature (London) **320**, 340 (1986).

[41] P. N. Pusey, W. van Megen, P. Bartlett, B. J. Ackerson, J. G. Rarity, and S. M. Underwood, Phys. Rev. Lett. **63**, 2753 (1989).

[42] Z. Cheng, W. B. Russel, and P. M. Chaikin, Nature (London) **401**, 893 (1999).

[43] J. Zhu, M. Li, R. Rogers, W. Meyer, R. H. Ottewill, S.-S. S. Crew, W. B. Russel, and P. M. Chaikin, Nature (London) **387**, 883 (1997).

[44] Z. Cheng, P. M. Chaikin, J. Zhu, W. B. Russel, and P. M. Meyer, Phys. Rev. Lett. **88**, 015501 (2002).

[45] E. Yablonovitch, Phys. Rev. Lett. **58**, 2059 (1987).

[46] S. John, Phys. Rev. Lett. **58**, 2486 (1987).

[47] M. M. Sigalas, C. M. Soukoulis, C. T. Chan, and D. Turner, Phys. Rev. B **53**, 8340 (1996).

[48] M. M. Sigalas, C. M. Soukoulis, C. T. Chan, R. Biswas, and K. M. Ho, Phys. Rev. B **59**, 12 767 (1999).

[49] Z.-Y. Li and Z.-Q. Zhang, Phys. Rev. B **62**, 1516 (2000).

[50] M. Bayindir, E. Cubukcu, I. Bulu, T. Tut, E. Ozbay, and C. M. Soukoulis, Phys. Rev. B **64**, 195113 (2001).

[51] J. Ballato, J. Dimaio, and A. James, Appl. Phys. Lett. **75**, 1497 (1999).

[52] Y. A. Vlasov, M. A. Kaliteevski, and V. V. Nikolaev, Phys. Rev. B **60**, 1555 (1999).

[53] M. Megens, J. E. G. J. Wijnhoven, Ad Lagendijk, and W. L. Vos, J. Opt. Soc. Am. B **16**, 1403 (1999).

[54] A. F. Koenderink, M. Megens, G. van Soest, W. L. Vos, and A. Lagendijk, Phys. Lett. A **268**, 104 (2000).

[55] J. Huang, N. Eradat, M. E. Raikh, and Z. V. Vardeny, Phys. Rev. Lett. **86**, 4815 (2001).

[56] H. Kosaka, T. Kawashima, A. Tomita, M. Notomi, T. Tamamura, T. Sato, and S. Kawakami, Phys. Rev. B **58**, R10 096 (1998).

[57] T. Ochiai and J. Sanchez-Dehesa, Phys. Rev. B **64**, 245113 (2001).

[58] A. Stein, Microporous Mater. **44−45**, 227 (2001).

[59] L. Samoilovich and M. Samoilovich (unpublished).

[60] V. M. Masalov, K. A. Aldushin, P. V. Dolganov, and G. A. Emel'chenko, Phys. Low-Dimens. Semicond. Struct. **5/6**, 45 (2001).

[61] S. Filin and A. Puzynin, Australian Gemologist **21**, 278 (2002).

[62] R. J. Carlson and S. Asher, Appl. Spectrosc. **38**, 297 (1984).

[63] The index of spheres $n_s = 1.33$ was determined in additional experiments in which the exact index matching (Ref. 2) condition

was determined by use of a set of infiltration liquids of differing refractive indices.

[64] A. L. Reynolds, Ph.D. thesis, University of Glasgow, 2000.

[65] A. Reynolds, F. Lopez-Tejeira, D. Cassagne, F. J. Garcia-Vidal, C. Joanin, and J. Sanchez-Daheza, Phys. Rev. B **60**, 11 422 (1999).

[66] The diffraction in front of the sample considered here is different from coherent backscattering of light (Refs. 54 and 55), which occurs in a very narrow cone $\sim 10^{-2}$ rad around the incident laser beam.

[67] W. H. Zachariasen, *Theory of X-Ray Diffraction in Crystals* (Dover, New York, 1945).

[68] In the particular case of specular reflectivity ($\alpha = \theta$) Eqs. (2) and (3) lead to the standard form of the Bragg law used in many studies of opals: $m\lambda = 2d(n^2 - \sin^2 \theta)^{1/2}$.

[69] The width of the stop band can be estimated either from reflectivity or transmission spectra in the single-crystal approximation without absorption.

[70] Each diffraction peak can be homogeneously broadened due to the finite thickness of the domains.

[71] The width of the stop band at the oblique incidence (FWHM$=40$ nm at $\theta = 30°$) is larger than at normal incidence (FWHM$=18$ nm, see Table I).

[72] In fact scattering occurs both in front of and behind the sample. However it is very difficult to detect light scattered in front of the sample since its intensity is dominated by the Bragg diffraction.

[73] For incidence along the normal ($\theta = 0$), the directions of the diffuse halo and the additional beam coincide. However, for $\theta \neq 0$, the diffuse halo remains centered around θ as expected, whereas the additional beam remains centered close to the normal, as observed in Fig. 7.

[74] It is interesting to note that in the spectra of scattering at very large angles ($\beta > 40°$) the shape of the background changes, exhibiting an increase of the intensity towards shorter wavelengths. This indicates the presence of wavelength-dependent Rayleigh-type scattering on smaller features with broader directionality which becomes visible against the reduced background at large β.

[75] H. C. van de Hulst, *Light Scattering by Small Particles*, 1st ed. (Dover, New York, 1981).

[76] A. Ishimaru, *Wave Propagation and Scattering in Random Media* (Academic, New York, 1978).

[77] J. D. Joannopoulos, R. D. Meade, and J. N. Winn, *Photonic Crystals* (Princeton University, Princeton, NJ, 1995).